Lanthanum-Doped Graphene for Electrocatalytic Reduction of Nitrogen Monoxide

Yu Yan, Zaheer Masood, Bin Wang*

School of Chemical, Biological and Materials Engineering, University of Oklahoma, Norman, OK 73019, United States

Email: wang_cbme@ou.edu

ABSTRACT

Electrocatalytic conversion of nitrogen oxides is a promising approach to address nitrogen pollution in underground water. Nitrogen oxides, such as nitrate and nitrite, can be reduced to N_2 and NH_3 over an electrocatalyst, with NO as the key intermediate, subsequent reaction of which controls the overall activity and selectivity. Here, we report density functional theory calculations of NO electrocatalytic reduction (NOER) over lanthanum embedded in graphene, through which we show that the localized states in La drives the reaction favorably, due to more pronounced molecular adsorption and charge transfer, than transition metals such as Co. The free energy profiles are compared between La-based single-atom catalyst (SAC) and Co-based SAC, for producing N_2 and NH_3. We find that La-SAC intensifies the electron transfer to the adsorbed NO, promoting the first protonation step of NO, which is the potential-limiting step on Co-SAC. Also, an intriguing effect of water solvent is revealed on La-SAC. In addition to stabilizing the intermediate species, water molecules that are coordinated with La participate directly in the protonation steps, enhancing the catalyst activity. This study reveals the unique mechanism of NOER over rare-earth-based catalysts, highlighting the potential application of atomically dispersed f-block elements for electrocatalytic reactions.

1. INTRODUCTION

Nitrogen pollution is one of the critical environmental challenges because of the extensive usage of nitrogen-rich fertilizer[1,2,3,4] and accumulated nitrogen in agricultural lands, which further converts to nitrate via biological nitrification[5]. The excess levels of nitrate have been observed in a vast amount of water bodies, becoming a pervasive problem in water quality, as nearly 23 million people are exposed to drinking water with above-regulated limits of nitrate[3]. This nitrate contamination in groundwater is a public health threat to human and can result in cancer and the blue-baby disease[2,6,7]. As a remedial solution, denitrification requires conversion of nitrate to a dischargeable product with minimal environmental impact[2]. Biological denitrification has been widely used; however, its capacity is limited by the operating condition of microorganisms[1,6,8]. Alternatively, chemical reduction has been considered an effective approach to convert nitrogen-containing species[5,6,9,10].

Among the chemical approaches, electrocatalysis enables a sustainable denitrification process when combined with renewable electricity[1,2,7,8,11]. Electroreduction of nitrite and nitric oxide has been investigated on a variety of metal surfaces such as Au, Ag, Cu, Ir, Ru, Rh, Pt, and Pd[5,9,11,12,13]. One of the best performance was reported on a Pt electrode[14,15], but its application is restricted by the expensive cost of the noble metal and its chemical stability. Meanwhile, many efforts have been devoted to understanding the reaction mechanism of the electrocatalytic reduction, particularly evolution of nitrogen-containing intermediates[1,2,5,7,8,11,12,16]. Electrocatalytic reduction of NO_3^- over Pt suggests that the surface-adsorbed NO is the key intermediate, controlling selectivity towards either N_2 or NH_3[9,11,16] and that NO accumulates as the reaction proceeds based on IR-based evidence[1,9,14,17].

Due to the maximum atom utilization efficiency and unique catalytic properties of atomically-dispersed metal atoms, single-atom catalyst (SAC) has been investigated as a feasible and efficient pathway for electrochemical conversion of nitrogen oxides[18,19,20,21,22]. Previous studies of electrocatalytic reduction of NO_3^- over SAC have revealed that reduction of NO, the key intermediate, is the critical step for nitrite reduction, consistent with reports on metal surfaces[18,19]. In the following discussion we focus on NO reduction, as it is the common kinetically relevant surface intermediate for reducing nitrite and nitrate and its reduction determines the product distribution. Previous studies show that d-block metal-based SACs are normally associated with a high overpotential for activating the surface-adsorbed NO[20,21,22]; for example, the proposed SAC based on Cu, Fe and Co has limiting potentials varied from 0.3 to 0.4 V[19,21,22].

Most previous studies of SAC-based electrocatalytic reduction of nitrogen oxides are focused on the d-p orbital coupling between d-block metal and nitrogen oxides. The emerging application of rare-earth (RE)-based SAC has been developed with great potentials in several electrocatalytic reactions[23,24,25,26,27,28] because of the distinct electronic properties of RE from d-block element; this includes the more localized 4f atomic orbital, large atom radii, pronounced spin-orbit coupling, high oxophilicity[29], and low electronegativity[23,24,29]. The unique electronic structure of 4f orbitals is also reported to promote charge transport[24,25,27]. Although many research have been performed to incorporate RE elements into nanostructured materials in the form of atomically dispersed single-atom site[25,26,27,28,30,31], a systematic study on the unique property of RE and its involvement in the electrocatalytic reduction in NO is still lacking.

Here, through density functional theory (DFT) calculations, we show that the La-SAC has distinct NOER activity, due to enhanced adsorption of NO and proton transfer, as compared to Co-SAC. As shown in literature, with similar N-doped structures, Co has the most favorable NO adsorption and reaction kinetics among the investigated d-block metal[32]. Thus, here we select Co-SAC as a useful benchmark to compare with RE-based SAC in NO reduction. The electrocatalytic activity was examined on N-doped graphene incorporated with single La or Co atom. The free energy diagram shows that La embedded in N-doped graphene promotes the first protonation step of NO, resulting from a strong polarization of NO, and that no apparent potential-limiting step could be identified. The density of states (DOS) analysis and charge transfer calculations provide an explanation for the enhanced activity of La-SAC, which is attributed to the intensified charge transfer from the metal to NO. The strong NO adsorption at La also leads to formation of dimers, creating an alternate path to produce N_2, which is unlikely on Co-SAC. We further show the role of water over both SACs. In addition to the effect of water to stabilize the protonated intermediates, the coordinated water on La-SAC also serves as a key proton doner. Due to the strong oxophilicity of La, water forms strong covalent bonds with the La-based SAC, leading to distinct coordination environment as compared to the Co-based SAC. These water molecules can participate directly in the reaction, facilitating the protonation steps. Overall, this study demonstrates La-based SAC as a promising candidate for electrocatalytic reduction of nitrogen oxides.

2. COMPUTATIONAL METHODS

The plane-wave DFT calculations were carried out using VASP[33,34,35]. The Perdew-Burke-Ernzerhof (PBE) functional[36] within the generalized gradient approximation (GGA)[36] was used for the exchange-correlation energy. Electron-ion interaction was described by the projector augmented wave (PAW) approach [37,38] and the van der Waals (vdW) interaction was included using the DFT-D3 method[39]. All electronic energies in calculations were converged within 10^{-5} eV, and the force on each atom was converged to below 0.02 eV $Å^{-1}$. We calculated a close-packed 5×5 graphene surface with 20 Å vacuum in the z-direction. The 3×3×1 Monkhorst-pack k-point mesh was used to sample the first Brillouin zone during structural optimization. The calculated lattices constants of La_2O_3 were used to determine the U value for La 4f states using the DFT + U method, and a value of 8.0 eV was applied. Using this U value, the band gap of La_2O_3 was calculated, and the obtained value of 3.9 eV agrees with the literature[24]. Charge transfer was calculated based on charge density difference and visualized using the VESTA[40]. The electronic transfer over SAC was analyzed by the Bader charge population.[41]

The single atoms were positioned at a di-vacancy of a 5 x 5 graphene supercell, which was created by removing two carbon atoms and replacing the four connecting carbons with N atoms. The formation energy (E_f) for the SAC was determined by the difference between the binding energy (E_b) and the cohesive energy (E_c).

$$E_f = E_b - E_c$$

$$\mathrm{E_b} = \mathrm{E_{total}} - \mathrm{E_{substrate}} - \mathrm{E_{TM}}$$

$$E_c = (E_{bulk} - nE_{TM})/n$$

Where $E_{total}, E_{substrate}, E_{TM}\ and\ E_{bulk}$ represent the total energies of the single metal in nitrogen-doped graphene, the substrate, the single metal adatom, and metal bulk, respectively.

The Gibbs free energy change of each elementary step was calculated using the model of the computational hydrogen electrode[42,43] where the chemical potential of $(H^+ + e^-)$ at pH = 0 is set to the chemical potential of 1 bar H_2 in the gas phase at 298 K. The Gibbs free energy values G can be obtained by

$$\mathrm{G} = \mathrm{E_{DFT}} + \mathrm{ZPVE} - \mathrm{T\Delta S} + \Delta \mathrm{G_U},$$[44]

where E_{DFT} is total energy from DFT calculations, $ZPVE\ and\ T\Delta S$ is the zero-point energy and entropy change at 298 K, respectively, derived from vibrational modes and statistical thermodynamics. ΔG_U is the free energy contribution obtained by the electrode potential U. The vibrational frequencies were calculated by fixing the system except the absorbate, four N atoms, and the metal. The overall entropy change ΔS consists of vibrational entropy S_{vib} and translational, rotational entropy $S_{trans+rot}$. The vibrational entropy S_{vib} was derived by DFT-calculated vibrational frequencies $\nu_{cal.}$. Some low-frequency vibrational modes (e.g., $\nu < 50$ cm^{-1}) may consist of hindered translation and rotation as shown by visualizing the corresponding atomic motions. Thus, two methods were employed: (i) all low-frequency modes round up to 50 cm^{-1} using VASPKIT[45] to estimate the entropy correction $T\Delta S *_{vib}$. (ii) we assumed the adsorbed spices remain a constant portion (1/3 used in this study) of the entropy of gaseous molecules.[46] In this case, the translational and rotational entropy at 298 K of the gas-phase molecules were determined by statistical methods or taken from the database. We find that the trend in the free energy diagram remains the same, and that the approach with rounded frequencies tends to stabilize all the surface species by 0.3-0.4 eV. The relative energy

difference in each elementary step is largely unaffected. The calculations reported here are obtained with the first approach if not specified.

The solvation effect in an aqueous solution was computed by two approaches - explicit solvation with one water molecule (i.e., the micro-solvation model) and the continuum solvation model (the implicit solvation) implemented in VASPsol[47,48]. We evaluated these two methods and compared their effects on the energy profile using Co-SAC (Figure S1). All intermediate species were stabilized by including solvation. The calculated overpotential could be reduced in both solvent models, and the implicit solvation reduced the limiting potential by 0.14 V, similar to 0.16 V using the explicit model. The solvation effects by including explicit water molecules are similarly reported in the literature[49,50]. The rest of the calculations were thus performed on explicit solvation with one additional water molecule.

The current study is based on computational hydrogen electrode approach[42]. We tried to calculate the energy profile for the first two protonation steps using a constant potential approach[51] and found similar results (see Figure S2). The computational details on constant potential calculations are included in the SI.

3. RESULTS AND DISCUSSION

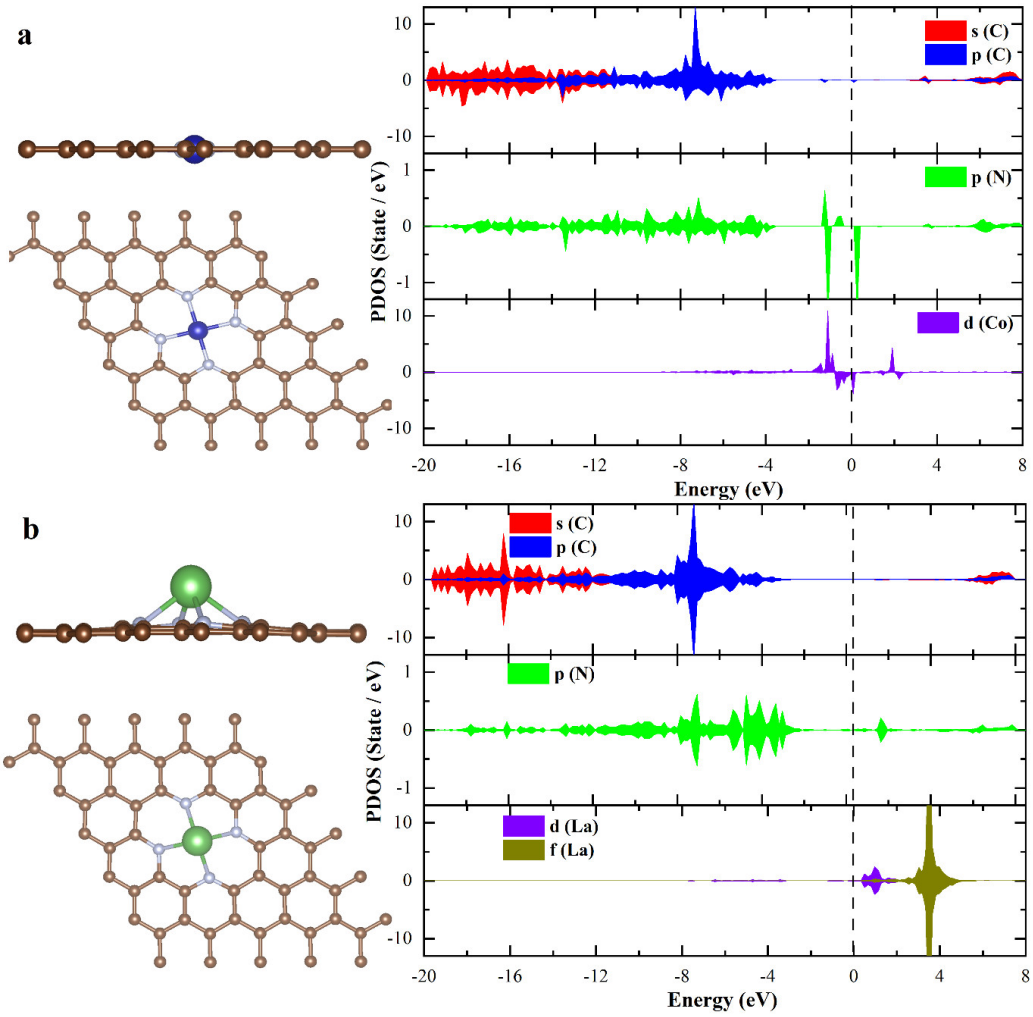

Figure 1. Comparison of the atomic structures and electronic properties of the Co- and La-SAC. (a) The optimized adsorption configuration of Co-SAC and PDOS of the substrate and the metal; (b) The optimized configurations and PDOS of La-SAC. Brown, silver, blue, and green balls represent C, N, Co, and La, respectively.

The formation energy was calculated for Co or La incorporated into N_4-Graphene. The values of E_f represent the thermodynamic trend for single atoms to aggregate into clusters versus binding to the substrate as single atoms. We find that the Co atom is attached to the

center of the vacancy (Figure 1) with a formation energy of –2.5 eV, while the La atom strongly adsorbs above the surface with a formation energy of –3.3 eV. It shows that both metals tend to be atomically dispersed on the substrate rather than aggregation to form the metal clusters. The projected density of states (PDOS) analysis is then used to analyze the hybridization state between the single atom and the substrate (Figure 1 and Figure S3). The Co single atom hybridizes with metal d orbitals and nitrogen p orbitals of N_4-graphene close to the Fermi energy. The CoN_4 moiety carries a magnetic moment of 0.69 μB, as shown by the asymmetric spin-up and spin-down states close to the Fermi energy (Figure 1a). In contrast, La-SAC does not carry any magnetic moment. The Bader charge analysis shows that La is oxidized to form La^{2+}, indicating a pronounced charge transfer between La and the substrate. The more localized La electronic states indicate weaker hybridization with the substrate, and its larger atomic size results in vertical displacement from the graphene plane. Similar electron transfer was reported on single La atom on graphitic carbon for the CO_2 reduction[27]. The different electronic occupation in La compared to Co leads to unique chemistry when interacting with oxygenates as discussed below.

The reactant NO adsorbs with two possible configurations: side-on with both N and O atoms involved in the bonding and end-on with only N atom forming a bond with the metal. We find that only the end-on configuration is accessible on the Co-SAC, similar to most transition metal-based SACs[19,22]. The adsorption energy is -1.9 eV (Table 1). The activation of NO on Co-SAC is manifested by the elongated N-O bond, which increases to 1.19 Å from 1.17 Å in the gas phase. Bader charge analysis in Figure 2 shows that 0.24 negative charge is accumulated in the NO molecule. Instead, NO adsorbs on La in both the end-on and side-on

configurations, with the same adsorption energy of -1.8 eV, comparable to NO adsorption on Co-SAC. The La-N bond length is 2.43 and 2.61 Å in the side-on and end-on configuration, respectively. The N-O bond is elongated to 1.22 or 1.26 Å is observed on La-SAC, indicating a more pronounced NO activation than it on Co-SAC. In addition, we find a more enhanced charge transfer for NO adsorption on La-SAC. That is, side-on NO gains 0.71 electrons in total. Compared to gas-phase NO, the N and O atoms upon adsorption carries 0.12 and 0.59 negative charges, respectively, transferred from the La-SAC. The NO adsorbed via the end-on configuration on La-SAC shows a very similar trend in charge transfer and bond length with the side-on configuration (Figure S5). Both the intensified negative charge and longer chemical bond imply a more activated NO and a feasible NOER activity over La-SAC.

Table 1. Adsorption energy and bond lengths upon NO adsorption on Co- and La-SAC.

SAC (Configuration)	Eads (eV)	Bond Length	
		N-Co/La (Å)	N-O (Å)
Co (End-on)	-1.9	1.80	1.19
La (Side-On)	-1.8	2.61	1.26
La (End-On)	-1.8	2.43	1.22

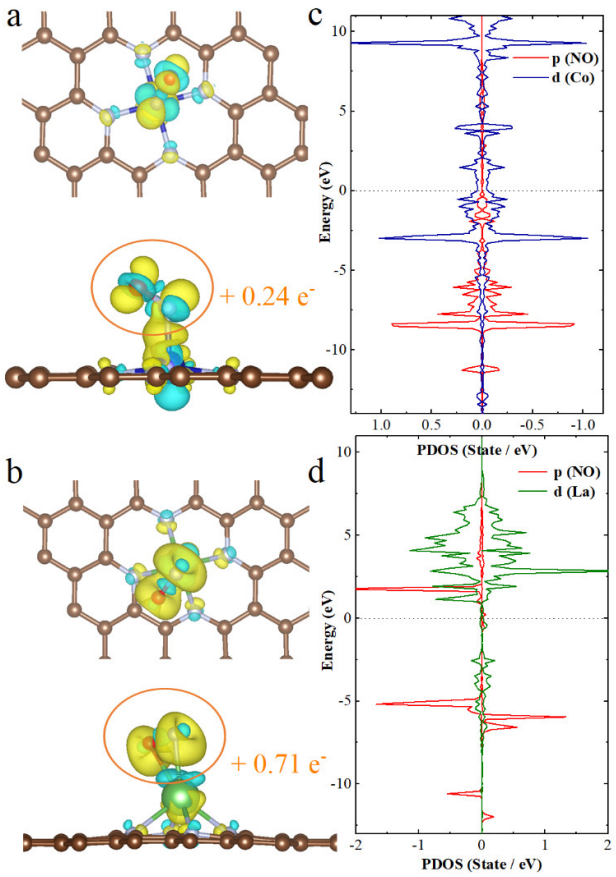

Figure 2. Comparison of the NO adsorption on the Co- and La-SAC. Charge density difference of NO adsorption on (a) Co- and (b) La-SAC. Bader charge on the NO is shown. The iso-surface value is set to 4×10^{-3} e/Å^3. The positive and negative values in yellow and cyan show electron accumulation and depletion, respectively. The PDOS of NO adsorbed on (c) Co-SAC and (d) La-SAC. Brown, silver, red, blue, and green balls represent C, N, O, Co, and La, respectively. PDOS analysis within a narrower energy window is included in Figure S4.

Further insight into NO adsorption on SACs is revealed in the PDOS analysis on NO p orbital and the metal d orbital (Figure 2). NO on Co-SAC with more hybridized and delocalized

p-states suggests a covalent adsorbate-catalyst interaction. The magnetic moment on Co-SAC disappears upon NO adsorption because the two unpaired electrons at Co-SAC and NO are now paired, leading to degenerate states. Instead, the NO p states remain localized on La-SAC, evidenced by the narrower states in Figure 2d. This analysis suggests an ionic bonding on La-SAC. The NO-La-SAC carries a magnetic moment of 1.9 μB, which results from the unpaired electron in P_y of NO and an addition electron transferred from the La-SAC to the P_z orbital of NO (Figure 2d). Thus, the La single atom in SAC can be considered La^{3+} upon the NO adsorption. The La-SAC has strong interactions with NO and water due to its strong oxophilicity, which was reported in the literature[29]. Thus, there is pronounced NOER activity difference as discussed below.

The mechanism of NOER has been studied extensively on metal catalysts and SAC. It is known that the product of NOER depends on the NO coverage. At a low coverage, the NO molecules adsorb on metal sites and follows sequential protonation to form NH_3 following $NO(g) + 5H^+ + 5e^- \rightarrow NH_3(l) + H_2O(l)$, where the first protonation is the potential-limiting step in DFT studies[18,21,22]. When the NO coverage increases, NO may adsorb as a dimer and be reduced to N_2 through an N_2O intermediate following $2NO(g) + 4H^+ + 4e^- \rightarrow N_2(g) + 2H_2O(l)$. N_2 can also be produced through the N-N coupling between adsorbed NO and partially hydrogenated species NH_x described by the equation $NH_2(ad) + NO(ad) \rightarrow N_2(g) + H_2O(l)$.

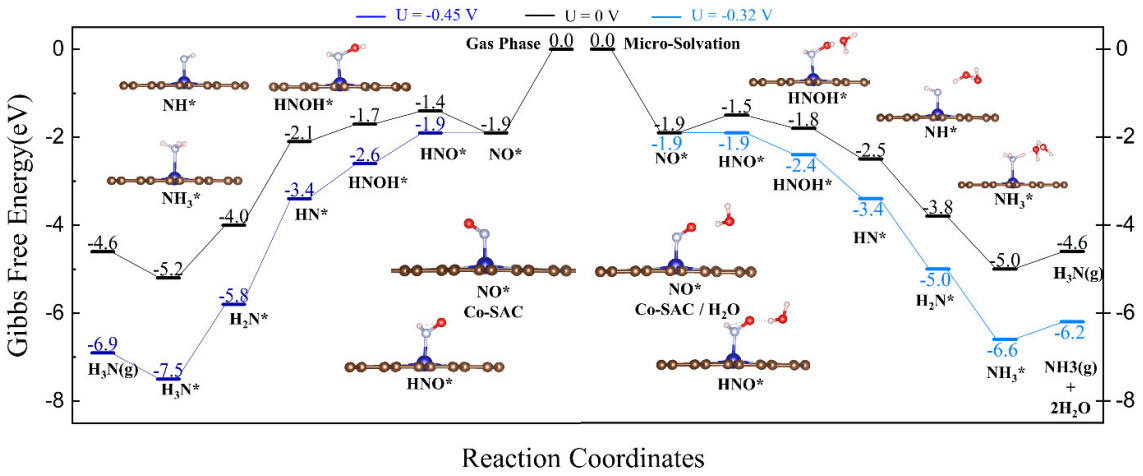

Figure 3. Calculated free energy diagram for NOER toward NH_3 over Co-SAC. The profile on Co-SAC following to the most favorable reduction pathway at pH = 0 in a gas-phase model is shown on the left panel and in a micro-solvation model on the right. The values for the first three protonation steps are included in Table S1 to show the calculation of the potential limiting step.

In the following, we first study the NOER initialized by NO unimolecular adsorption on Co- and La-SAC. As shown in Figure S6, in the absence of water solvent, the key intermediate HNO* is more thermodynamically stable than NOH*, in good agreement with literature studies[19,22]. The NOER reaction follows the sequence of NO, HNO, HNOH, NH, NH_2, and NH_3. We also tested the species H_2NO* and H_2NOH* but found they were less energetically favorable (Figure S6). The complete NOER diagram on Co-SAC is shown in Figure 3; the NOER on Co-SAC is limited by the first protonation step, which demands an electrode potential of -0.45 V to eliminate the uphill energy difference. Meanwhile, the desorption of NH_3 is energetically difficult in the gas phase, similar to molecular desorption over many noble metal-based SAC[21], requesting 0.6 eV desorption energy on Co-SAC. The desorption is much

easier in the water solvent as discussed later in the text.

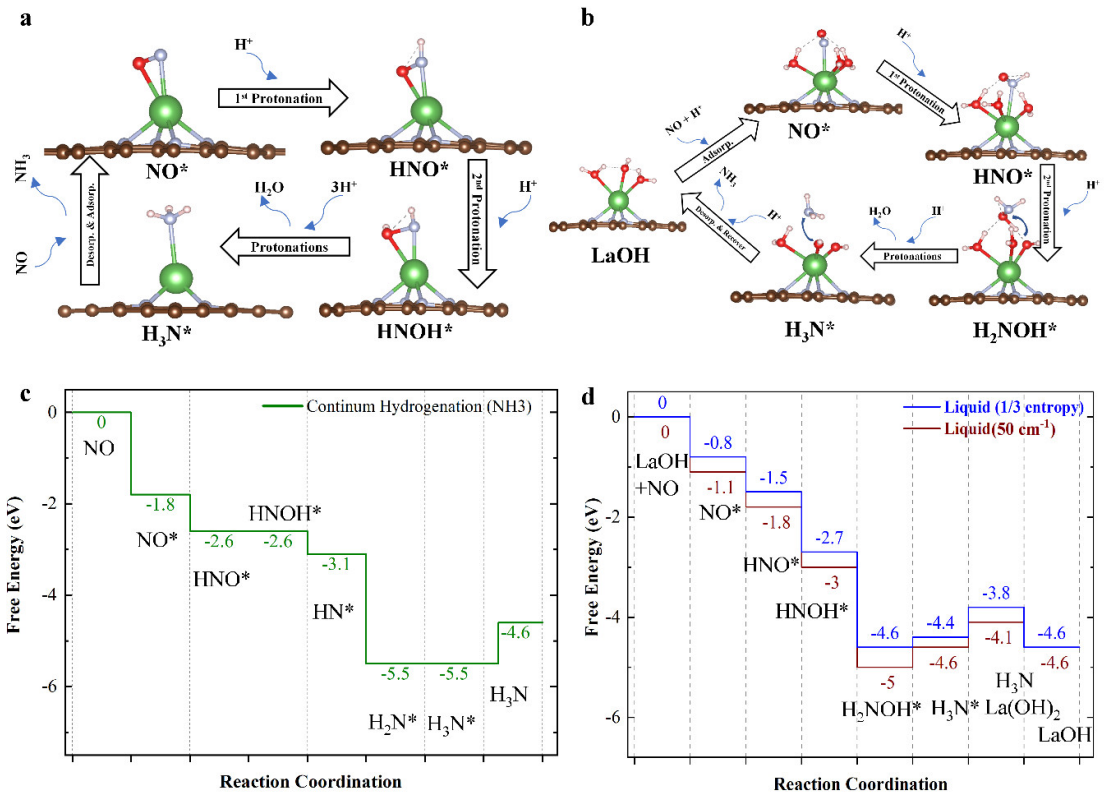

Figure 4. Calculated free energy diagram for NOER toward NH_3 over La-SAC. (a) and (c) The configuration of NOER species on La and free energy diagram of NOER toward NH_3 on La-N_4-graphene catalyst without considering water. (b) and (d) NOER configurations and free energy diagrams using micro=solvation. Two different methods to calculate the entropic contribution are compared in (d).

A similar NOER path was investigated on La-SAC (Figure 4a). No obvious uphill step was observed on the formation of HNO* or other steps, except the last desorption of NH_3 (Figure

4c). This trend in NO reduction is distinct from Co-SAC. The feasibility of HNO* on La-SAC can be attributed to the intensive charge transfer to NO from La. As evidenced in the PODS and magnetic moment calculations in Figure 2, the adsorbed NO molecule is electron rich on La, driving the occurrence of protonation. On La-SAC, the sequential hydrogenation follows HNO, HNOH, NH, NH_2, and finally NH_3, which then desorbs. No uphill steps were observed for the overall path in the absence of an electrode potential. Despite the desorption step of NH_3 with an energy cost of 0.6 eV energy cost, the solvation energy of NH_3 may reduce the energy cost, similar to it on Co-SAC.

In heterogeneous catalysis, the role of waters is critical in many different ways and in a variety of reactions[9,52,53]. For example, the interaction between surface species and water could be responsible for lowering the activation energy of the rate-limiting step and enhancing the catalytic activity. Here, we investigated the interfacial reaction in NOER by introducing an explicit water molecule. On Co-SAC, it is found the water is weakly bound to Co-SAC; the adsorption energy is -0.23 eV. Since NO adsorption is strongly favored at Co-SAC, the pre-adsorbed H_2O is thus replaced upon NO adsorption. This water is then tightly bind with the NO adsorbate, forming a H-bond, and other reactive intermediates formed along the pathway. We find that this H-bonding stabilizes each intermediate in NOER to a similar extent. As shown in Figure 3, the solvent brings 0.1 to 0.3 eV energy gain in the NOER elementary steps on Co-SAC. The limiting potential (i.e., to form HNO) is reduced by 0.13 V when water forms a H-bond with HNO* in this micro-solvation model. Also, the energy cost of NH_3 desorption decreased by 0.5 eV when the solvation was applied.

The role of water is particularly pronounced over La-SAC. On La-SAC, the water solvent

has strong interaction with the La-SAC. Multiple H_2O molecules co-adsorb at La-SAC because of the high oxophilicity of La and open space for adsorption. We found that three H_2O could attach to La-SAC, forming $La(H_2O)_3$ with adsorption energy for each H_2O around -0.8 eV (Figure S7). Besides, the water dissociation to form La-OH is favorable under zero external potential. The first water dissociation in $La(H_2O)_3$ forms $La(OH)(H_2O)_2$ with an additional energy gain of -0.59 eV. However, deprotonation of the second and the third water is endothermic, requiring 0.58 and 1.74 eV reaction energy, respectively. The Bader charge analysis show more positive charge localized at the hydrated La center than the pristine La-SAC, due to the formation of this hydroxide group.

On the hydrated La-SAC site, NOER follows a similar reaction path shown in Figure 4b. NO is reduced to HNO* followed by HNOH*, similar to the NOER mechanism on the pristine La-SAC. Once the HNOH* species is formed, it simultaneously abstracts a proton from a La-bonded water, forming H_2NOH*. The remaining H_2O considerably stabilize the H_2NOH species, different from the NOER intermediate on a clean La-SAC. The exothermic reaction indicates that formation of the H_2NOH intermediate is feasible. This new intermediate observed on hydrated La suggests a prevalent solvent effect that provides an excellent stabilization for certain polar chemical species. Upon another protonation step, the N-O bond in H_2NOH dissociates to form NH_2. The hydration on La-SAC offers a strong driving force on this sequential hydrogenation mechanism. We find that the $LaOH(H_2O)_2$ favors transferring one more hydrogen to NH_2*, producing NH_3*. The hydrated La-SAC undergoes another protonation step to close the catalytic cycle, recovering the active site to $LaOH(H_2O)_2$. This step is slightly endothermic with an 0.2 eV energy cost. In the presence of water, in

addition to stabilizing the reactive species on $LaOH(H_2O)_2$, the solvent saturates the hydration of La and participates in the reaction acts as a proton source. There are no uphill elementary steps observed in NOER on La-SAC in this micro-solvent model.

We further calculated the hydrogen binding energy over Co-SAC, La-SAC, and hydrated La-SAC (i.e., $La(OH)(H_2O)_2$) shown on Figure S8.. Over the La-based SAC, the hydrogen binding energy is more positive that it on the Co-SAC, which suggests improved selectivity toward NOER over La-based SACs.

Before moving on to discuss reactions to form N_2, here we briefly discuss the entropic contribution. Using two ways to include the entropy effect, the NOER free energy profile on $La(OH)(H_2O)_2$ is displayed in Figure 4d. In one method, the low frequency (< 50 cm^{-1}) modes were all rounded up to a particular value (50 cm^{-1}), while in the other, 1/3 entropy loss of gas-phase molecule was assumed upon adsorption. Using the second approach assuming adsorbed NO maintains 2/3 gaseous translational and rotational entropy, the adsorption energy of NO is -0.8 eV. The NO adsorption is more feasible in the first approach with an additional 0.3 eV energy gain. In the NOER free energy diagram, this is generally true that all the surface species are stabilized by 0.3 eV with the first approach. Therefore, the reaction energies remain the same for all the elementary steps, except adsorption and desorption.

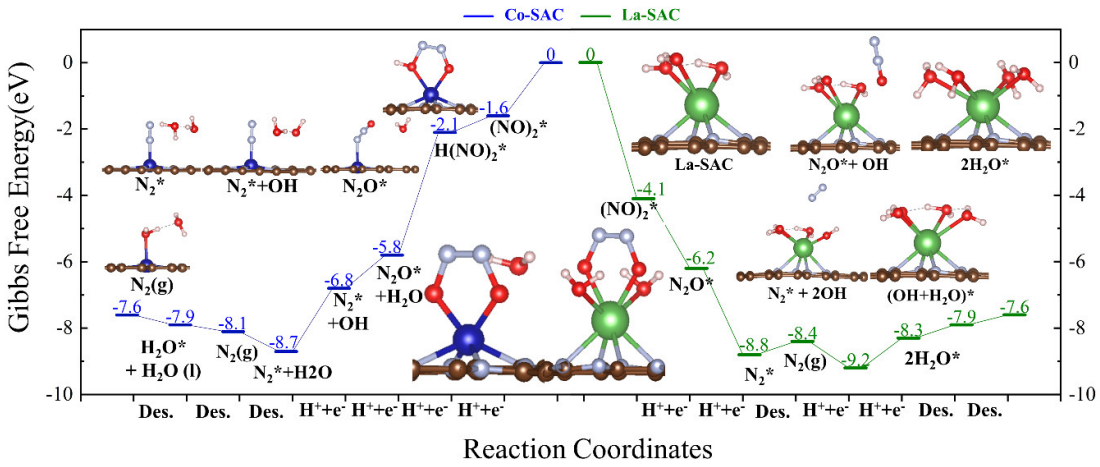

Figure 5. Free energy diagram of NOER toward N_2 at pH=0. The profile on Co (left half) and La (right half) are compared.

In the following, we discuss the alternative reaction path of NOER toward N_2. In the proposed mechanisms on Pt, highly feasible N_2 formation could result from N-N coupling between N-containing surface species.[11] The NOER mechanism on SAC toward N_2 starts with NO bimolecular adsorption. $(NO)_2$ has a weak bond between two N atoms within the molecule. The metal site interacts with the two O atoms in the NO dimer, forming a five-membered ring. The structure of $(NO)_2$ adsorption and its reduction on Co- and La-SAC are displayed in Figure 5. The dimer $(NO)_2$ is highly stabilized over La-SAC. The adsorption energy per NO is -2.1 eV, about the same as the single NO adsorption. Such strong binding can be attributed to the strong oxophilicity of La-SAC. The bimolecular adsorption energy on Co-SAC is -0.8 eV per NO, which is weaker than single NO adsorption (-1.6 eV). Due to this less favorable $(NO)_2$ adsorption on Co, the bimolecular adsorption on Co-SAC could only be observed when the NO concentration is very high. The reduction of $(NO)_2$ to N_2 includes four proton-electron steps. The protons are added to O sequentially, forming $H(NO)_2$, N_2O+H_2O, and N_2+2H_2O. Each N-

O bond cleavage produces a water molecule at the end. The catalytic cycle is completed with the desorption of N_2 and water molecules. The free energy diagram of $(NO)_2$ reduction on Co-SAC shows no uphill steps except the desorption step. It is anticipated that NH_3 is still the major product as co-adsorption of two NO is less likely on Co-SAC.

Over La-SAC, La starts with a hydrated configuration $LaOH(H_2O)_2$. To allow the NO bimolecular adsorption, a protonation to the OH on La is needed to desorb a water molecule to accommodate $(NO)_2$ adsorption. The adsorption is still exothermic even though it replaces one water molecule. The dissociation of N-O bonds in $(NO)_2$ is favorable on La after a protonation step to N. The N-O bond dissociation produces N_2O and OH directly. N_2O is not fully attached to La. We find that reduction of N_2O to N_2 is feasible in the protic environment and easily desorb from the SAC with an almost neutral energy profile. This hydrated La-SAC thus promotes both NH_3 and N_2 production.

It should be noted that the SAC defects, such as those generated during pyrolysis, may affect the electronic structure of the graphene and performance of the catalyst. For example, presence of the structural defects can tune the charge localization on the carbon and also the coordination between the metal center and the carbon host[27,54,55]. The exact local bonding configuration and coordination of La can be tuned by enlarging the vacancies in graphene, which provides more flexibility for introducing additional functional groups[27,54]. In addition, the reaction mechanism may vary depending on the active sites, as the latter determine the stability of different species over the surface, such as NOH on metal-free but defect-rich graphene[55] and HNO over metal and Co-SAC[21,32,50]. The exact reaction mechanism (and the dominate surface species) is thus determined by the active sites; It will be valuable to compare

the calculated results with experiments over well-controlled samples. This versatile tunability can in principle be leveraged to control the electronic structure of the single atoms in experiments.

4. CONCLUSIONS

We investigated electrocatalytic reduction of NO over La-SAC and compared its activity with a well-studied Co-SAC. The La-SAC shows distinct chemical bonding with NO due to its strong oxophilicity and unique coordination environment. Water has strong interaction with La-SAC forming a hydrated active site. Besides stabilization of the polar intermediates, the co-adsorbed water can participate in the reaction by proton transfer to the intermediate species. Unlike the formation of HNO as the potential-limiting step on Co-SAC and most other transition metal, no obvious potential-limiting step was observed on La-SAC. Due to the feasibility of co-adsorption two NO molecules, N_2 production is also more favorable on La-SAC than Co-SAC. This study thus opens a path for future work to explore the rare earth elements in the application of electrochemical reactions of oxygenates.

ASSOCIATED CONTENT

The Supporting Information is available free of charge on the ACS Publication website. Total energy diagram of NOER over Co-SAC with different solvent models; Constant potential methodology and results; additional DOS figures; NO adsorbs in an end-on configuration on La-SAC; DFT calculations of the hydrated La-SAC structure.

AUTHOR INFORMATION

Corresponding Author

*Email: wang_cbme@ou.edu

ORCID

Zaheer Masood: 0000-0003-2836-3754

Bin Wang: 0000-0001-8246-1422

Notes

The authors declare no competing financial interest.

ACKNOWLEDGMENTS

The DFT calculations were performed at the OU Supercomputing Center for Education & Research and the National Energy Research Scientific Computing Center (NERSC), a U.S. Department of Energy Office of Science User Facility. The work was supported by the U.S. Department of Energy, Basic Energy Sciences, Catalysis Science (Grant DE-SC0018284).

REFERENCES

1. Duca, M.; Koper, M. T., Powering denitrification: the perspectives of electrocatalytic nitrate reduction. *Energy & Environmental Science* **2012,** *5* (12), 9726-9742.

2. Heck, K. N.; Garcia-Segura, S.; Westerhoff, P.; Wong, M. S., Catalytic Converters for Water Treatment. *Accounts of Chemical Research* **2019,** *52* (4), 906-915.

3. Burow, K. R.; Nolan, B. T.; Rupert, M. G.; Dubrovsky, N. M., Nitrate in groundwater of the United States, 1991− 2003. *Environmental science & technology* **2010,** *44* (13), 4988-4997.

4. Resasco, D. E.; Wang, B.; Sabatini, D., Distributed processes for biomass conversion could aid UN Sustainable Development Goals. *Nat Catal* **2018,** *1* (10), 731-735.

5. Rosca, V.; Duca, M.; de Groot, M. T.; Koper, M. T., Nitrogen cycle electrocatalysis. *Chemical Reviews* **2009,** *109* (6), 2209-2244.

6. Prüsse, U.; Hähnlein, M.; Daum, J.; Vorlop, K.-D., Improving the catalytic nitrate reduction. *Catalysis Today* **2000,** *55* (1), 79-90.

7. Barrabés, N.; Sá, J., Catalytic nitrate removal from water, past, present and future perspectives. *Applied Catalysis B: Environmental* **2011,** *104* (1-2), 1-5.

8. Martínez, J.; Ortiz, A.; Ortiz, I., State-of-the-art and perspectives of the catalytic and electrocatalytic reduction of aqueous nitrates. *Applied Catalysis B: Environmental* **2017,** *207*, 42-59.

9. Huang, P.; Yan, Y.; Banerjee, A.; Lefferts, L.; Wang, B.; Albanese, J. A. F., Proton shuttling flattens the energy landscape of nitrite catalytic reduction. *Journal of Catalysis* **2022,** *413*, 252-263.

10. Wang, P.; Liu, G.; Hao, Z.; Zhang, H.; Li, Y.; Sun, W.; Zheng, L.; Zhan, S., In situ formation of cocatalytic sites boosts single-atom catalysts for nitrogen oxide reduction. *Proc*

Natl Acad Sci U S A **2023,** *120* (8), e2216584120.

11. Garcia-Segura, S.; Lanzarini-Lopes, M.; Hristovski, K.; Westerhoff, P., Electrocatalytic reduction of nitrate: Fundamentals to full-scale water treatment applications. *Applied Catalysis B: Environmental* **2018,** *236*, 546-568.

12. Liu, J.-X.; Richards, D.; Singh, N.; Goldsmith, B. R., Activity and Selectivity Trends in Electrocatalytic Nitrate Reduction on Transition Metals. *ACS Catalysis* **2019,** *9* (8), 7052-7064.

13. Choi, J.; Du, H.-L.; Nguyen, C. K.; Suryanto, B. H. R.; Simonov, A. N.; MacFarlane, D. R., Electroreduction of Nitrates, Nitrites, and Gaseous Nitrogen Oxides: A Potential Source of Ammonia in Dinitrogen Reduction Studies. *ACS Energy Letters* **2020,** *5* (6), 2095-2097.

14. Rosca, V.; Koper, M. T. M., Mechanism of Electrocatalytic Reduction of Nitric Oxide on Pt(100). *The Journal of Physical Chemistry B* **2005,** *109* (35), 16750-16759.

15. Katsounaros, I.; Figueiredo, M. C.; Chen, X.; Calle-Vallejo, F.; Koper, M. T., Structure- and coverage-sensitive mechanism of NO reduction on platinum electrodes. *ACS Catalysis* **2017,** *7* (7), 4660-4667.

16. Xu, P.; Agarwal, S.; Lefferts, L., Mechanism of nitrite hydrogenation over Pd/ γ -Al2O3 according a rigorous kinetic study. *Journal of catalysis* **2020,** *383*, 124-134.

17. Zhao, Y.; Rao, N. K.; Lefferts, L., Adsorbed species on Pd catalyst during nitrite hydrogenation approaching complete conversion. *Journal of catalysis* **2016,** *337*, 102-110.

18. Niu, H.; Zhang, Z.; Wang, X.; Wan, X.; Shao, C.; Guo, Y., Theoretical Insights into the Mechanism of Selective Nitrate-to-Ammonia Electroreduction on Single-Atom Catalysts. *Advanced Functional Materials* **2020,** *31(11)*, 2008533.

19. Wu, Z.-Y.; Karamad, M.; Yong, X.; Huang, Q.; Cullen, D. A.; Zhu, P.; Xia, C.; Xiao,

Q.; Shakouri, M.; Chen, F.-Y.; Kim, J. Y.; Xia, Y.; Heck, K.; Hu, Y.; Wong, M. S.; Li, Q.; Gates, I.; Siahrostami, S.; Wang, H., Electrochemical ammonia synthesis via nitrate reduction on Fe single atom catalyst. *Nature Communications* **2021,** *12* (1), 2870.

20. Qu, W.; Liu, X.; Chen, J.; Dong, Y.; Tang, X.; Chen, Y., Single-atom catalysts reveal the dinuclear characteristic of active sites in NO selective reduction with NH3. *Nature Communications* **2020,** *11* (1), 1532.

21. Wu, Q.; Wei, W.; Lv, X.; Wang, Y.; Huang, B.; Dai, Y., Cu@g-C3N4: An Efficient Single-Atom Electrocatalyst for NO Electrochemical Reduction with Suppressed Hydrogen Evolution. *The Journal of Physical Chemistry C* **2019,** *123* (51), 31043-31049.

22. Wang, Z.; Zhao, J.; Wang, J.; Cabrera, C. R.; Chen, Z., A Co–N4 moiety embedded into graphene as an efficient single-atom-catalyst for NO electrochemical reduction: a computational study. *Journal of Materials Chemistry A* **2018,** *6* (17), 7547-7556.

23. Kaiser, S. K.; Chen, Z.; Faust Akl, D.; Mitchell, S.; Pérez-Ramírez, J., Single-Atom Catalysts across the Periodic Table. *Chemical Reviews* **2020,** *120* (21), 11703-11809.

24. Gu, W.; Song, Y.; Liu, J.; Wang, F., Lanthanum-Based Compounds: Electronic Band-Gap-Dependent Electrocatalytic Materials for Oxygen Reduction Reaction. *Chemistry – A European Journal* **2017,** *23* (42), 10126-10132.

25. Wang, X.; Tang, Y.; Lee, J.-M.; Fu, G., Recent advances in rare-earth-based materials for electrocatalysis. *Chem Catalysis* **2022**, 2(5), 967-1008.

26. Liu, J.; Kong, X.; Zheng, L.; Guo, X.; Liu, X.; Shui, J., Rare Earth Single-Atom Catalysts for Nitrogen and Carbon Dioxide Reduction. *ACS Nano* **2020,** *14* (1), 1093-1101.

27. Chen, P.; Lei, B.; Dong, X. a.; Wang, H.; Sheng, J.; Cui, W.; Li, J.; Sun, Y.; Wang, Z.;

Dong, F., Rare-earth single-atom La－N charge-transfer bridge on carbon nitride for highly efficient and selective photocatalytic CO2 reduction. *ACS nano* **2020,** *14* (11), 15841-15852.

28. Zhang, N.; Yan, H.; Li, L.; Wu, R.; Song, L.; Zhang, G.; Liang, W.; He, H., Use of rare earth elements in single-atom site catalysis: A critical review—Commemorating the 100th anniversary of the birth of Academician Guangxian Xu. *Journal of Rare Earths* **2021,** *39* (3), 233-242.

29. Kepp, K. P., A quantitative scale of oxophilicity and thiophilicity. *Inorganic chemistry* **2016,** *55* (18), 9461-9470.

30. Zheng, B.; Fan, J.; Chen, B.; Qin, X.; Wang, J.; Wang, F.; Deng, R.; Liu, X., Rare-earth doping in nanostructured inorganic materials. *Chemical Reviews* **2022,** *122* (6), 5519-5603.

31. Xiong, H.; Xie, J.; Dong, J., Insight into rare earth yttrium and nitrogen co-decorated graphene as a promising material for NOx detection. *Physics Letters A* **2020,** *384* (35), 126910.

32. Wang, Z.; Zhao, J.; Wang, J.; Cabrera, C. R.; Chen, Z., A Co－N 4 moiety embedded into graphene as an efficient single-atom-catalyst for NO electrochemical reduction: a computational study. *Journal of Materials Chemistry A* **2018,** *6* (17), 7547-7556.

33. Kresse, G.; Furthmüller, J., Efficient iterative schemes for ab initio total-energy calculations using a plane-wave basis set. *Physical review B* **1996,** *54* (16), 11169.

34. Kresse, G.; Furthmüller, J., Efficiency of ab-initio total energy calculations for metals and semiconductors using a plane-wave basis set. *Computational materials science* **1996,** *6* (1), 15-50.

35. Kresse, G.; Hafner, J., Ab initio molecular-dynamics simulation of the liquid-metal－amorphous-semiconductor transition in germanium. *Physical Review B* **1994,** *49* (20), 14251.

36. Perdew, J. P.; Burke, K.; Ernzerhof, M., Generalized gradient approximation made simple. *Physical review letters* **1996,** *77* (18), 3865.

37. Blöchl, P. E., Projector augmented-wave method. *Physical review B* **1994,** *50* (24), 17953.

38. Kresse, G.; Joubert, D., From ultrasoft pseudopotentials to the projector augmented-wave method. *Physical review b* **1999,** *59* (3), 1758.

39. Grimme, S.; Antony, J.; Ehrlich, S.; Krieg, H., A consistent and accurate ab initio parametrization of density functional dispersion correction (DFT-D) for the 94 elements H-Pu. *The Journal of chemical physics* **2010,** *132* (15), 154104.

40. Momma, K.; Izumi, F., VESTA 3 for three-dimensional visualization of crystal, volumetric and morphology data. *Journal of applied crystallography* **2011,** *44* (6), 1272-1276.

41. Tang, W.; Sanville, E.; Henkelman, G., A grid-based Bader analysis algorithm without lattice bias. *Journal of Physics: Condensed Matter* **2009,** *21* (8), 084204.

42. Nørskov, J. K.; Rossmeisl, J.; Logadottir, A.; Lindqvist, L.; Kitchin, J. R.; Bligaard, T.; Jónsson, H., Origin of the Overpotential for Oxygen Reduction at a Fuel-Cell Cathode. *The Journal of Physical Chemistry B* **2004,** *108* (46), 17886-17892.

43. Rossmeisl, J.; Logadottir, A.; Nørskov, J. K., Electrolysis of water on (oxidized) metal surfaces. *Chemical Physics* **2005,** *319* (1), 178-184.

44. Skúlason, E.; Bligaard, T.; Gudmundsdóttir, S.; Studt, F.; Rossmeisl, J.; Abild-Pedersen, F.; Vegge, T.; Jónsson, H.; Nørskov, J. K., A theoretical evaluation of possible transition metal electro-catalysts for N2 reduction. *Physical Chemistry Chemical Physics* **2012,** *14* (3), 1235-1245.

45. Wang, V.; Xu, N.; Liu, J.-C.; Tang, G.; Geng, W.-T., VASPKIT: A user-friendly interface

facilitating high-throughput computing and analysis using VASP code. *Computer Physics Communications* **2021,** *267*, 108033.

46. Campbell, C. T.; Sellers, J. R. V., Correction to Enthalpies and Entropies of Adsorption on Well-Defined Oxide Surfaces: Experimental Results. *Chemical Reviews* **2013,** *113* (8), 6902-6902.

47. Mathew, K.; Sundararaman, R.; Letchworth-Weaver, K.; Arias, T.; Hennig, R. G., Implicit solvation model for density-functional study of nanocrystal surfaces and reaction pathways. *The Journal of chemical physics* **2014,** *140* (8), 084106.

48. Mathew, K.; Kolluru, V. S. C.; Mula, S.; Steinmann, S. N.; Hennig, R. G., Implicit self-consistent electrolyte model in plane-wave density-functional theory. *The Journal of Chemical Physics* **2019,** *151* (23), 234101.

49. Zou, X.; Liu, M.; Wu, J.; Ajayan, P. M.; Li, J.; Liu, B.; Yakobson, B. I., How Nitrogen-Doped Graphene Quantum Dots Catalyze Electroreduction of CO2 to Hydrocarbons and Oxygenates. *ACS Catalysis* **2017,** *7* (9), 6245-6250.

50. Huang, P.; Yan, Y.; Banerjee, A.; Lefferts, L.; Wang, B.; Faria Albanese, J. A., Proton shuttling flattens the energy landscape of nitrite catalytic reduction. *Journal of Catalysis* **2022,** *413*, 252-263.

51. Choi, C.; Gu, G. H.; Noh, J.; Park, H. S.; Jung, Y., Understanding potential-dependent competition between electrocatalytic dinitrogen and proton reduction reactions. *Nature Communications* **2021,** *12* (1), 1-11.

52. Li, G.; Wang, B.; Resasco, D. E., Solvent Effects on Catalytic Reactions and Related Phenomena at Liquid-Solid Interfaces. *Surface Science Reports* **2021**, 100541.

53. Li, G.; Wang, B.; Resasco, D. E., Water-Mediated Heterogeneously Catalyzed Reactions. *ACS Catalysis* **2020,** *10* (2), 1294-1309.

54. Zhu, M.; Zhao, C.; Liu, X.; Wang, X.; Zhou, F.; Wang, J.; Hu, Y.; Zhao, Y.; Yao, T.; Yang, L.-M., Single atomic cerium sites with a high coordination number for efficient oxygen reduction in proton-exchange membrane fuel cells. *ACS Catalysis* **2021,** *11* (7), 3923-3929.

55. Huang, L.; Cheng, L.; Ma, T.; Zhang, J. J.; Wu, H.; Su, J.; Song, Y.; Zhu, H.; Liu, Q.; Zhu, M., Direct Synthessis of Ammonia From Nitrate On Amorphous Graphene With Near 100% Efficiency. *Advanced Materials* **2023**, 2211856.

For Table of Contents Use Only